Volume 1 | Number 1 | Jan 2013 | Pages 1–100

Nanoscale

www.rsc.org/nanoscale

ROYAL SOCIETY
OF CHEMISTRY

ROYAL SOCIETY
OF CHEMISTRY

www.rsc.org/nanoscale

Engineering electronic properties of layered transition-metal dichalcogenide compounds through alloying

Alex Kutana, Evgeni S. Penev, and Boris I. Yakobson

Department of Materials Science and Nanoengineering, Rice University, Houston, TX 77005

Abstract

Binary alloys present a promising venue for band gap engineering and tuning of other mechanical and electronic properties of materials. Here we use the density-functional theory and cluster expansion to investigate the thermodynamic stability and electronic properties of 2D transition metal dichalcogenide (TMD) binary alloys. We find that mixing electron-accepting or electron-donating transition metals into 2D TMD semiconductors leads to degenerate p- or n-doping, respectively, effectively rendering them metallic. We then proceed to investigate the electronic properties of semiconductor-semiconductor alloys. The exploration of the configurational space of the 2D molybdenum-tungsten disulfide ($Mo_{1-x}W_xS_2$) alloy beyond the mean field approximation yields insights into anisotropy of the electron and hole effective masses in this material. The effective hole mass in the 2D $Mo_{1-x}W_xS_2$ is nearly isotropic and is predicted to change almost linearly with the tungsten concentration x. In contrast, the effective electron mass shows significant spatial anisotropy. The values of the band gap in 2D $Mo_{1-x}W_xS_2$ and $MoSe_{2(1-x)}S_{2x}$ are found to be configuration-dependent, exposing the limitations of the mean field approach to band gap analysis in alloys.

Introduction

Recent advances in the synthesis of 2D transition metal dichalcogenides (TMDs) sparked new interest in these materials. Due to the constraint of reduced dimensionality, 2D materials have properties that often exceed those of their bulk counterparts,[1] making them promising candidates for use in faster and more efficient electronic devices.[2,3] Unlike semi-metallic graphene, many 2D TMDs are semiconductors, and thus are more suitable than graphene to be used as electronic switches. In addition, some interesting effects and phenomena are observed in TMDs that are not present in graphene, the most striking of which are superconductivity, charge density waves, and Mott insulator states.[4–6]

The most recent revival of interest in 2D TMDs is connected with a new method of synthesis by liquid exfoliation.[7] In total, there exist ~60 TMD compounds, 2/3 of which have layered structure[8] and in principle could exist in the 2D form. The initial seminal work[7] produced many new 2D TMDs, including MoS_2, WS_2, $MoSe_2$, $MoTe_2$, $TaSe_2$, $NbSe_2$, $NiTe_2$, BN, and Bi_2Te_3. Since then, even more 2D TMD compounds have been prepared by liquid exfoliation. A recent review lists a large number of two-dimensional transition metal dichalcogenides that have been synthesized to date.[9] This variety of synthesized 2D TMDs holds promise for designing materials and devices with custom electronic and mechanical properties. By using alloys of two or more of these materials one could achieve an even greater flexibility and access an almost continuous range of properties.

In this work, we explore the varying electronic properties of TMD alloys with constituent concentration, including the carrier effective mass and band gap. Qualitatively, the electronic properties of TMDs are determined by the localization behavior of the d-bands of the transition metal.[8] Depending on the degree of localization, these materials can be insulators, semiconductors, semimetals, or metals. The degree of the d state mixing depends on the nature of the transition metal and its chalcogen ligand environment, and is expected to be influenced by their substitutions in an alloy. Here, our purpose is to determine the extent to which the band structure is perturbed by alloy substitutions. In particular, we look at whether these changes occur continuously or abruptly.

Several 2D TMD alloys have recently been reported experimentally, including $Mo_{1-x}W_xS_2$,[10,11] $MoSe_{2(1-x)}S_{2x}$,[12] and $Nb_{1-x}W_xS_2$.[13] One alloy ($Mo_{1-x}W_xS_2$) indicates substitutional disorder,[10] suggesting that

an extensive analysis of configurational space is needed. Recently, an effort to explore the configurational space of 2D alloys has been made by applying cluster expansion (CE) method to 2D boron pseudoalloy.[14] The role of the mixing species was played by the vacancy sites. As a result of the exhaustive structure search, a complete set of all thermodynamically stable phases of 2D boron has been found.[14] Recent theoretical work on alloying of 2D TMDs included analyses based on introducing several representative alloy structures[15] and as well as the CE approach[16] that accounts for the full configurational entropy. In this work, we apply CE methodology to 2D TMDs, and consider regular substitutional alloys of several common 2D TMDs.

Methods and Theory

The cluster expansion (CE) method[17] provides an effective way to sample a 2^N-dimensional configuration space of an N-site binary alloy. Unlike mean field approximations, the CE method gives the full microscopic description of atomic configurations in a crystal. In the CE formalism, any function f of a given configuration $\boldsymbol{\sigma} = \{\sigma_1, \sigma_2, \ldots, \sigma_N\}$ of spins σ_i on N lattice sites is fitted through a multivariate expansion in site occupancy variables (spins) σ_i. In an alloy, the roles of spin variables are played by chemical identities of different atomic species. The cluster expansion of the mixing energy $E(\boldsymbol{\sigma})$ can be written as:[17]

$$E(\boldsymbol{\sigma}) = \sum_{\alpha, s} E_{\alpha s} \Phi_{\alpha s}(\boldsymbol{\sigma}) \tag{1}$$

where $E_{\alpha s}$ are the expansion coefficients and $\Phi_{\alpha s}(\boldsymbol{\sigma})$ are so-called characteristic cluster functions defined for all possible distinct subsets (clusters) $\alpha = \{p, p', \ldots, p''\}$ of the points of the full lattice. The sets $s = \{n, n', \ldots, n''\}$ in the sum Eq.1 include all possible non-zero indices of orthonormal polynomials entering the definition of cluster functions $\Phi_{\alpha s}(\boldsymbol{\sigma})$. Zero-index orthonormal polynomials have the value of 1, and therefore do not need to be included into the sum.

In case of a two-component alloy, the cluster expansion of the mixing energy (per site) can be written as:[18]

$$E(\boldsymbol{\sigma}) = \sum_{\alpha} m_\alpha J_\alpha \left\langle \prod_{i \in \alpha_{eq}} \sigma_i \right\rangle \tag{2}$$

Here, lattice symmetry has been taken into account by forming symmetry-adapted expansion coefficients for equivalent clusters. Like in the general case, α in Eq. 2 enumerates all lattice-symmetry inequivalent subsets (clusters) of a full set of lattice sites, m_α is the number of clusters that are equivalent to α by the lattice symmetry (divided by the total number of lattice sites N), and coefficients J_α are the effective cluster interactions (ECI). Angle brackets designate the arithmetic average over all sets of points $i = \{q, q', \ldots, q''\}$ that are equivalent to the subset represented by α through lattice symmetry. The averaging over the symmetry-equivalent clusters is possible due the independence of the effective cluster interactions J_α on the spin configurations in case of a two-component system. This averaging reduces the number of independent ECI coefficients. The discrete site occupation variables σ_i are usually assigned the values of $+1$ and -1 in a binary system.

The cluster expansion Eq.2 converges rapidly with cluster size, yielding an exact result in the untruncated form. In this work, the CE fitting of the mixing energy and search for the thermodynamic ground state was carried out with the Alloy-Theoretic Automated Toolkit (ATAT) code.[18] The quality of the CE fit was evaluated using a cross-validation score.[19] The formation energies of alloy structures generated by ATAT and used in the fitting procedure were computed at the density-functional theory

(DFT) level. Total energies and band structures were obtained within the local spin density approximation (LSDA) with projector-augmented wave (PAW) potentials, as implemented in VASP.[20] The plane-wave cutoff was 520 eV in all calculations, and spin-orbit coupling was neglected.

Results

Alloy lattice matching

There is a general tendency for group 4–7 metal dichalcogenides to form layered structures, in contrast to group 8–10 metals, like pyrites, which prefer nonlayered structures.[8] Here, we mostly consider layered group 4–7 metal dichalcogenides. Single-layer 2D TMDs can in turn form two polymorphs, having either octahedral (1T), or trigonal prismatic (2H) metal coordination geometries. Despite their structural similarity, layered TMDs display a great variety of electronic properties.

In order to select viable candidates for binary alloys, we considered pairs of TMD compounds that matched a set of predefined conditions based on specific descriptors and rules. The descriptors and rules that were used in the selection reflected the requirements of a good match in the lattice constant and metal-chalcogen bond distance, as well as the band gap constraints. Mixtures of two metallic TMDs were not expected to display a finite band gap, and were excluded by the rules. During the alloy selection, the following rules were imposed:

$$|a_1 - a_2|/\max\{a_1, a_2\} < 0.034 \,,$$
$$\Delta d_{M-X} < 0.1 \,\text{Å} \,,$$
$$(E_{g1} > 0) \vee (E_{g2} > 0) \,. \tag{3}$$

Here, a_1 and a_2 are the lattice constants of the two TMD materials, E_{g1}, E_{g2} are their band gaps, and Δd_{M-X} is the difference in the metal-chalcogen bond distance. The first and second rules reflect the requirements that the mismatch of the lattice constants between the two materials be smaller than 3%, and the difference in metal-chalcogen bond distance be less than 0.1 Å, respectively, whereas the third rule requires that at least one of the compounds be a semiconductor.
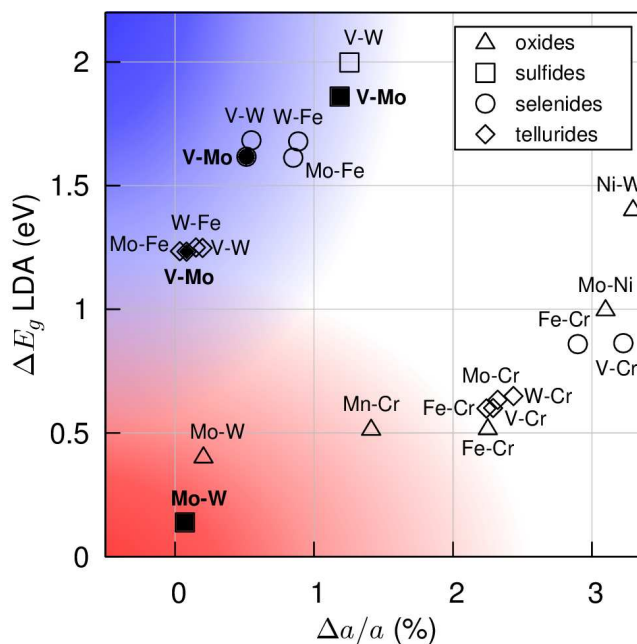
Figure 1. Lattice constant matching for metal-metal pairs of 2H TMDs based on the LSDA lattice constants. Triangles designate oxides, squares – sulfides, circles– selenides, and diamonds – tellurides. The shaded area in the upper left corner of the plot is populated with vanadium-molybdenum and vanadium-tungsten dichalcogenides, which are metal-semiconductor alloys. The shaded area in the lower left corner contains semiconductor-semiconductor alloys of molybdenum and tungsten dichalcogenides. Bold labels and filled symbols designate compounds that were studied here using CE.

Figure 1 shows pairs of compounds that were selected based on these rules, plotted according to their differences in theoretical band gaps and mismatch of the lattice constants. The data points in the upper left corner of Fig. 1 correspond to the largest difference in band gaps, as well as the smallest lattice mismatch, potentially indicating the most favorable pairs. The upper left corner of the plot is populated with vanadium-molybdenum and vanadium-tungsten dichalcogenides. These materials represent alloys between a metal (VX_2) and a semiconductor (MoX_2, WX_2).

We found that these types of metal-semiconductor alloys are degenerate semiconductors at all mixings attained in calculations. The doping mechanism was determined to be *p*-type, through accepting an electron by the electron-deficient group-5 metal. Generally, when mixing the electron-deficient V (as well as other group-5 metals, such as Nb, and Ta) with group-6 semiconductors such as CrX_2, MoX_2, or WX_2, X=(O, S, Se, Te), the decrease in the number of electrons leads to metallic behavior and the shift of the Fermi level into the valence band. The degenerate *p*-doping behavior was observed in all of the aforementioned compounds studied at four different concentrations, and also in $V_{1-x}Mo_xTe_2$, $V_{1-x}Mo_xS_2$, and $V_{1-x}Mo_xSe_2$, which were studied in more detail at various concentrations and configurations with CE. From the CE calculations, $V_{1-x}Mo_xTe_2$ was found to be nominally energetically stable, whereas $V_{1-x}Mo_xS_2$ and $V_{1-x}Mo_xSe_2$ were determined energetically unstable, although mixing energies were rather small in all cases.
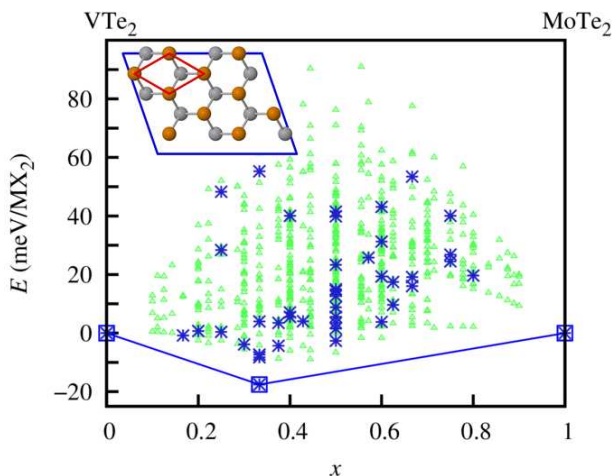

Figure 2. Mixing energies per MX_2 structural unit of the $V_{1-x}Mo_xTe_2$ alloy in the 2H phase. Large blue (dark) stars represent the values obtained from DFT calculations, and small green (light) triangles represent the values from the CE fitting. The solid line is the convex hull of the alloy thermodynamic ground state. The inset shows the largest supercell that was used in CE calculations as well as the unit cell of the 2H trigonal prismatic phase.

The results of the CE calculation for the $V_{1-x}Mo_xTe_2$ alloy in the 2H phase are shown in Fig. 2. The mixing energies are slightly negative, with absolute values on the order of 10-20 meV per MX_2 unit. These low values indicate that facile mixing should be possible at all concentrations. The positive mixing energies of $V_{1-x}Mo_xS_2$ and $V_{1-x}Mo_xSe_2$ are on the order of 10-20 meV per MX_2 unit. We also note that our CE approach uses the total energies of the DFT ground states, thus assessing the stability of these structures in the thermodynamic limit and at zero temperature. In cases of the low mixing energies, such as ones encountered here, the entropy contribution to the total free energy may be comparable to or even greater than the relative energy of mixing at the typical temperatures ~1000K used in the growth of these

structures. In the future, electronic excited states and phonon contributions may be taken into consideration to account for finite temperature effects in these materials.

The doping mechanism responsible for the metallic behavior in these alloys is illustrated in Fig. 3. Spin-polarized density of states (DOS) of the $V_{1-x}Mo_xTe_2$ alloy is shown at four different concentrations. As the concentration of V increases, the Fermi level moves deeper into the valence band. In terms of the conventional picture of the semiconductor doping, this shift corresponds to heavy doping of $MoTe_2$ with V impurities, resulting in a Mott semiconductor-metal transition. Similarly, the shift of the Fermi level into the conduction band may occur by heavy *n*-doping. For instance, our calculations show that increasing the number of electrons by mixing electron-donating Fe into a hypothetical 2H CrX_2 compound leads to metallicity by this mechanism. The 2H $CrSe_2$ is predicted to be a semiconductor with a small LDA band gap. After addition of 25% iron, the electronic DOS remains nearly unchanged, whereas the Fermi level is moved by ~0.3 eV into the conduction band. Similarly, in MoS_2 doped with 25% iron, the Fermi level resides ~0.5 eV above the edge of the conduction band (these mechanisms are complementary to the mechanically-induced semiconductor-metal transition that was proposed recently for the bilayer TMDs[21]).
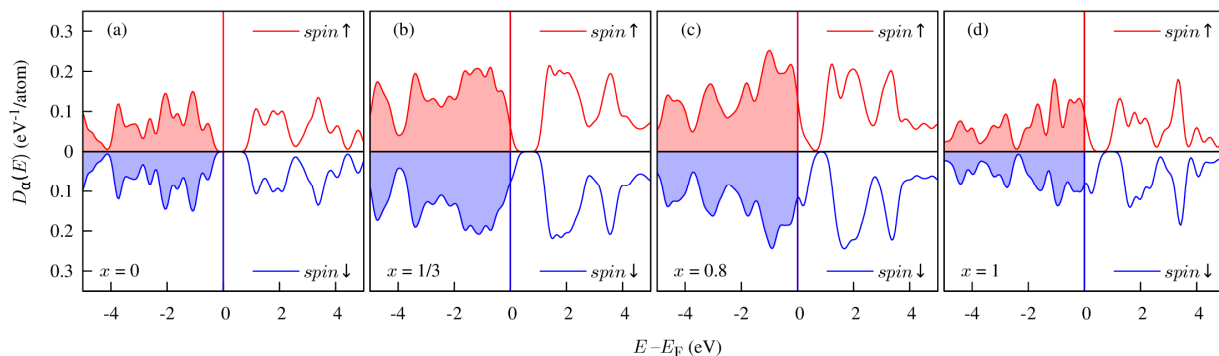

Figure 3. Spin-projected density of states showing the shifting of the Fermi level into the valence band of a metal-semiconductor alloy. The DOS of 2H $V_xMo_{1-x}Te_2$ alloy, at V concentration of 0% (a), 33% (b), 80% (c) and 100% (d) are shown. Atom configurations in (a), (c), and (d) correspond to the lowest energy thermodynamic states as predicted by the CE, whereas the structure at (b) is above the lowest thermodynamic state. The zero of the energy corresponds to the Fermi level.

Semiconductor-semiconductor alloys

Unlike alloys between metals and semiconductors, semiconductor-semiconductor alloys have finite band gaps at all concentrations. This property ensures *a priori* that the alloy is a semiconductor, but may be deemed as a disadvantage due to inability to decrease the alloy band gap below a certain fixed value. This latter possibility may be vital for applications where low energy electronic excitations are important, such as in infrared sensors. The range of possible variations of the band gap is also generally more limited than in case of a metal-semiconductor alloy.

In Fig. 1, a group of Mo-W dichalcogenide semiconductor-semiconductor alloys is located at the bottom left corner of the plot, indicating good lattice matching and moderate band gap variation with concentration. In this group, we focus on the properties of the $Mo_{1-x}W_xS_2$ alloy – a compound consisting of two of the most studied 2D TMDs. Both MoS_2 and WS_2 single-layer materials have been extensively characterized before. Several recent experimental[10,22] and theoretical[15,16] studies of their alloys exist. The latter employ analyses based on several representative structures,[15] as well as more detailed approaches including full configurational entropy.[16] Mixing energies and the convex hull of alloy ground states of $Mo_{1-x}W_xS_2$ are shown in Fig. 4. The alloy is found to be stable, with mixing energies on the order of -5 meV/MX_2 unit. Three distinct regions of concentrations can be delineated, viz. (1) $0 < x \lesssim 0.33$, (2) $0.33 \lesssim x \lesssim 0.60$, and (3) $0.60 \lesssim x < 1$. In the first region, the mixing energy decreases linearly with tungsten concentration. In the second region, the energy is almost independent from the concentration, whereas in

the third region the energy varies linearly again. According to the standard interpretation of the binary alloy phase diagram, the first and third regions correspond to domains of complete miscibility between the two components, whereas the second region is the polymorphic domain. Earlier, polymorphism was theoretically predicted in 2D boron,[14] implying that it would lead to a greater degree of disorder during synthesis. Here, polymorphism is displayed in the range of W concentrations $0.33 \lesssim x \lesssim 0.60$, and disorder is also more likely to exist in that range.

Both 2D MoS_2 and WS_2 constituents are direct-gap semiconductors,[23] with their valence band maximum (VBM) and conduction band minimum (CBM) located at the K point of the Brillouin zone. This suggests that their binary alloy may have a direct band gap at the same location. Our calculations confirm this assumption, finding a direct gap at the K point of the folded Brillouin zone in *all* mixed compounds.
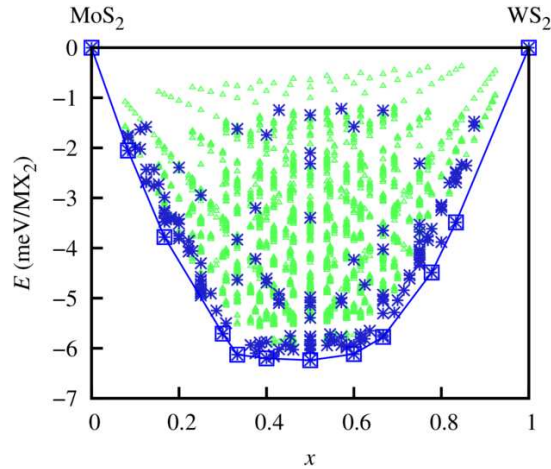

Figure 4. Mixing energies per MX_2 structural unit of the $Mo_{1-x}W_xS_2$ alloy in the 2H phase. Large blue (dark) stars represent the values obtained from DFT calculations, and small green (light) triangles represent the values from the CE fitting. The solid line is the convex hull of the alloy thermodynamic ground state.

We proceed with the calculation of the effective carrier mass in the $Mo_{1-x}W_xS_2$ alloy at the K point as a function of the alloy structure and composition. The tensor of the reciprocal effective carrier mass near the band edge for the energy dispersion law $\varepsilon = \varepsilon(\mathbf{k})$ is given by:[24]

$$\left(m^{*-1}\right)_{ij} = \frac{1}{\hbar^2}\frac{d^2\varepsilon}{dk_i dk_j} \tag{4}$$

The tensors of reciprocal effective masses $\left(m^{*-1}\right)_{ij}$ for holes and electrons were calculated from the parabolic fitting of $\varepsilon(\mathbf{k})$ near the VBM and CBM, respectively. Figure 5a shows the calculated effective hole masses in the $Mo_{1-x}W_xS_2$ alloy as a function of W concentration x, obtained by diagonalizing the reciprocal effective mass tensor $\left(m^{*-1}\right)_{ij}$. In some structures, the energies at the band edge are degenerate, giving rise to two types of carriers. In Fig. 5a, masses for the heavy and light holes in the principal axes are shown with open symbols, whereas nondegenerate cases are shown with filled symbols. One observes that the effective hole masses in the $Mo_{1-x}W_xS_2$ alloy vary almost linearly with x in nondegenerate cases. There is also little spatial anisotropy. In case of degenerate values, deviations from the linear trend are larger, while their spatial anisotropy is still quite small.

Unlike the effective hole masses, the effective electron masses in the $Mo_{1-x}W_xS_2$ alloys shows great directional anisotropy, as shown in Fig. 5b. As before, the values for heavy and light carriers are plotted with open symbols, whereas nondegenerate values are plotted with filled symbols. In some structures, the effective mass anisotropy reaches values as high as 2. Large increase of the effective mass

is observed in the $[11\bar{2}0]$ direction, while in the $[\bar{1}100]$ direction the linear trend is followed more closely. These disparities are testable and should be reflected as a marked difference in the behavior of two carrier types in alloys prepared under typical experimental conditions. Since currently there is no precise control over exact placement of atoms in an alloy, measurements of effective masses of electrons in $Mo_{1-x}W_xS_2$ should yield values that vary from one sample to another, even at the same mixing ratio. These variations should be interpreted by experimentalists as an intrinsic property of the system caused by the strong dependence of the effective mass on microscopic atomic configuration, and not a consequence of, e.g. faulty equipment or inadequate sample quality. On the other hand, effective hole masses should follow a linear trend very closely with concentration, displaying a narrow distribution around an average value at every concentration.

       The stark contrast in the effective mass anisotropy of the two carrier types is most likely related to orbital symmetry. Site orbital projections reveal that both the VBM and CBM Kohn-Sham wavefunctions are formed from the d orbitals of transition metal atom. However, the symmetries of these d orbitals are different. The top of the valence band wavefunction has $d_{xy} + d_{x^2-y^2}$ character, whereas the wavefunction at the bottom of the conduction band has d_{z^2} character. This assignment coincides with the splitting pattern predicted by the crystal field theory[25] for the perturbing field with trigonal prismatic symmetry. It follows that a band at the CBM that is formed from a single d_{z^2} orbital is more sensitive to the scattering by substituted atoms than the band at the VBM.
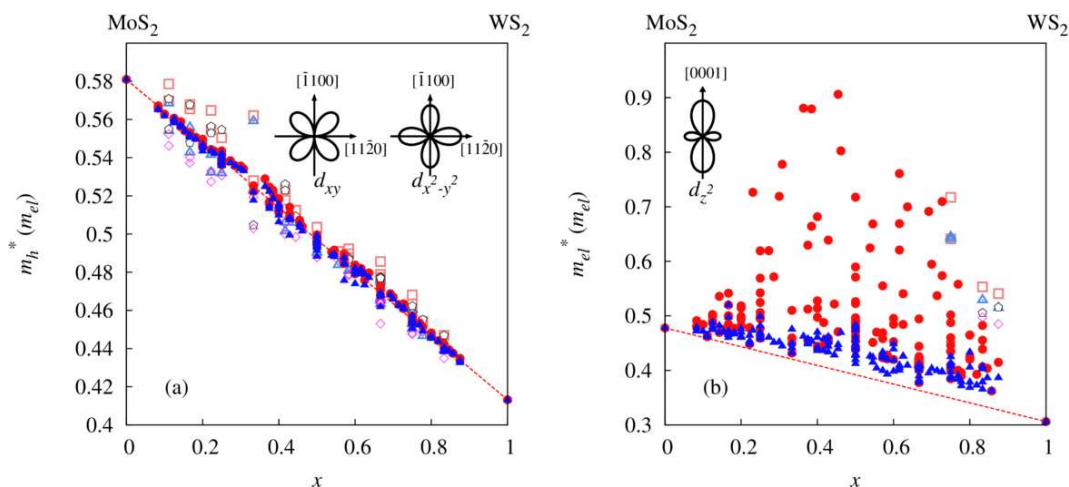

Figure 5. Calculated LDA effective masses of holes (a) and electrons (b) in the $Mo_{1-x}W_xS_2$ alloy as a function of W concentration x. Principal axes values for the heavy and light carriers in degenerate bands are shown with open symbols, whereas nondegenerate values are shown with filled symbols. Note the difference in scale in (a) and (b). Orbital drawings show the symmetry character of the Kohn-Sham states at the edges of corresponding bands.

       We next examine band gap variations as a function of x in $Mo_{1-x}W_xS_2$, as well as another similar semiconductor-semiconductor compound, $MoSe_{2(1-x)}S_{2x}$. Cluster expansion of the formation energy of $MoSe_{2(1-x)}S_{2x}$ (not shown) predicts it to be a thermodynamically stable compound, with mixing energies on the order of -8 meV per structural MX_2 unit. Figure 6 shows the calculated band gaps for these two compounds at various concentrations, as determined for structures used in CE calculations. The band gaps in the thermodynamic ground states are shown with larger symbols. The LDA gap varies from 1.87 to 2.0 eV in $Mo_{1-x}W_xS_2$ with concentration. These values are surprisingly close to the experimentally reported variation[11] from 1.85 to 1.99 eV in this alloy. Such a good agreement is probably coincidental and a result of the mutual cancellation of various many-body corrections and the effect of spin-orbit coupling (SOC) on the optical band gap. In $MoSe_{2(1-x)}S_{2x}$, the calculated band gap varies from 1.62 to 1.86 eV. Again,

these values compare very favorably with the experimentally measured variations between 1.55 and 1.87 eV.[12] The general trend of gradual band gap change between these two limiting values is clearly visible. However, in $Mo_{1-x}W_xS_2$, the gap stays nearly constant up to a W concentration of 0.5 and starts increasing afterwards, whereas in $MoSe_{2(1-x)}S_{2x}$ the gap variation is more uniform and nearly linear throughout the whole range of S concentrations. Overall, from the point of view of phenomenological description of semiconductor alloys, the band gaps in these compounds show slight bowing with a positive bowing parameter. In addition, band gaps should display configuration-dependent variations that can be observed in optical absorption or emission experiments. These variations should be interpreted as an intrinsic property of these alloys. The determined trends of band gap variations help set the important limits on their possible values and may be instrumental in the future design of 2D alloy-based devices.
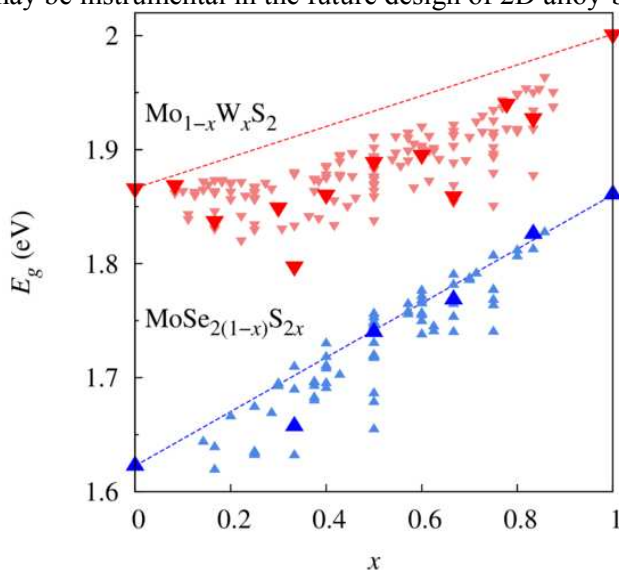

Figure 6. LDA band gaps in $Mo_{1-x}W_xS_2$ (downward triangles, red) and $MoSe_{2(1-x)}S_{2x}$ (upward triangles, blue) alloys as a function of concentration x. The band gaps in the thermodynamic ground states are shown with larger symbols.

Conclusions

We studied the thermodynamic stability and electronic properties of 2D transition metal dichalcogenide alloys using density-functional theory and cluster expansion formalism. Metal-semiconductor and semiconductor-semiconductor alloys were considered. Metal-semiconductor alloys were found to be always metallic, the doping mechanism being either through the degenerate electron or through hole doping by the metallic component. Among semiconductor-semiconductor alloys, we examined effective carrier masses in the thermodynamically stable $Mo_{1-x}W_xS_2$. In this compound, we found that the spatial anisotropy for holes is at most 4% at all concentrations, whereas for electrons the ratio of effective masses along the principal axes reached values as high as 2 in some structures. In this and another stable semiconductor-semiconductor 2D alloy, $MoSe_{2(1-x)}S_{2x}$, we calculated LDA band gaps as a function of concentration and found almost linear variation with slight bowing.

Acknowledgements

References

(1)   Splendiani, A.; Sun, L.; Zhang, Y.; Li, T.; Kim, J.; Chim, C.-Y.; Galli, G.; Wang, F. *Nano Lett* **2010**, *10*, 1271–1275.
(2)   Radisavljevic, B.; Radenovic, A.; Brivio, J.; Giacometti, V.; Kis, A. *Nat Nanotechnol* **2011**, *6*, 147–150.
(3)   Wang, Q. H.; Kalantar-Zadeh, K.; Kis, A.; Coleman, J. N.; Strano, M. S. *Nat Nanotechnol* **2012**, *7*, 699–712.
(4)   Gabovich, A. M.; Voitenko, A. I.; Ausloos, M. *Phys Rep* **2002**, *367*, 583–709.

(5)   Withers, R. L.; Wilson, J. A. *J Phys C* **1986**, *19*, 4809–4845.

(6)   Sipos, B.; Kusmartseva, A. F.; Akrap, A.; Berger, H.; Forró, L.; Tuti\vs, E. *Nat Mater* **2008**, *7*, 960–965.

(7)   Coleman, J. N.; Lotya, M.; O'Neill, A.; Bergin, S. D.; King, P. J.; Khan, U.; Young, K.; Gaucher, A.; De, S.; Smith, R. J.; Shvets, I. V.; Arora, S. K.; Stanton, G.; Kim, H.-Y.; Lee, K.; Kim, G. T.; Duesberg, G. S.; Hallam, T.; Boland, J. J.; Wang, J. J.; Donegan, J. F.; Grunlan, J. C.; Moriarty, G.; Shmeliov, A.; Nicholls, R. J.; Perkins, J. M.; Grieveson, E. M.; Theuwissen, K.; McComb, D. W.; Nellist, P. D.; Nicolosi, V. *Science* **2011**, *331*, 568–571.

(8)   Wilson, J. A.; Yoffe, A. D. *Adv Phys* **1969**, *18*, 193–335.

(9)   Chhowalla, M.; Shin, H. S.; Eda, G.; Li, L.-J.; Loh, K. P.; Zhang, H. *Nat Chem* **2013**, *5*, 263–275.

(10) Dumcenco, D. O.; Kobayashi, H.; Liu, Z.; Huang, Y.-S.; Suenaga, K. *Nat Commun* **2013**, *4*, 1351.

(11) Liu, H.; Antwi, K. K. A.; Chua, S.; Chi, D. *Nanoscale* **2014**, *6*, 624.

(12) Mann, J.; Ma, Q.; Odenthal, P. M.; Isarraraz, M.; Le, D.; Preciado, E.; Barroso, D.; Yamaguchi, K.; von Son Palacio, G.; Nguyen, A.; Tran, T.; Wurch, M.; Nguyen, A.; Klee, V.; Bobek, S.; Sun, D.; Heinz, T. F.; Rahman, T. S.; Kawakami, R.; Bartels, L. *Adv. Mater.* **2013**, n/a–n/a.

(13) Hoshyargar, F.; Sahoo, J. K.; Tahir, M. N.; Yella, A.; Dietzsch, M.; Natalio, F.; Branscheid, R.; Kolb, U.; Panthöfer, M.; Tremel, W. *Dalton Trans* **2013**.

(14) Penev, E. S.; Bhowmick, S.; Sadrzadeh, A.; Yakobson, B. I. *Nano Lett* **2012**, *12*, 2441–2445.

(15) Komsa, H.-P.; Krasheninnikov, A. V. *J Phys Chem Lett* **2012**, *3*, 3652–3656.

(16) Kang, J.; Tongay, S.; Li, J.; Wu, J. *J. Appl. Phys.* **2013**, *113*, 143703.

(17) Sanchez, J. M.; Ducastelle, F.; Gratias, D. *Phys. A* **1984**, *128*, 334–350.

(18) Van de Walle, A.; Asta, M.; Ceder, G. *Calphad* **2002**, *26*, 539–553.

(19) Van de Walle, A.; Ceder, G. *J Phase Equilibria* **2002**, *23*, 348–359.

(20) Kresse, G.; Furthmüller, J. *Phys Rev B* **1996**, *54*, 11169.

(21) Bhattacharyya, S.; Singh, A. K. *Phys Rev B* **2012**, *86*, 075454.

(22) Chen, Y.; Xi, J.; Dumcenco, D. O.; Liu, Z.; Suenaga, K.; Wang, D.; Shuai, Z.; Huang, Y.-S.; Xie, L. *ACS Nano* **2013**, *7*, 4610–4616.

(23) Ataca, C.; Sahin, H.; Ciraci, S. *J Phys Chem C* **2012**, *116*, 8983–8999.

(24) Kittel, C. *Introduction to solid state physics*; Wiley: New York, 1986.

(25) Bethe, H. *Ann Phys* **1929**, *3*, 133–208.